

Deep Learning to Accelerate Scatterer-to-Field Mapping for Inverse Design of Dielectric Metasurfaces

Maksym V. Zhelyeznyakov, Steve Brunton, and Arka Majumdar*

Cite This: <https://dx.doi.org/10.1021/acsp Photonics.0c01468>

Read Online

ACCESS |



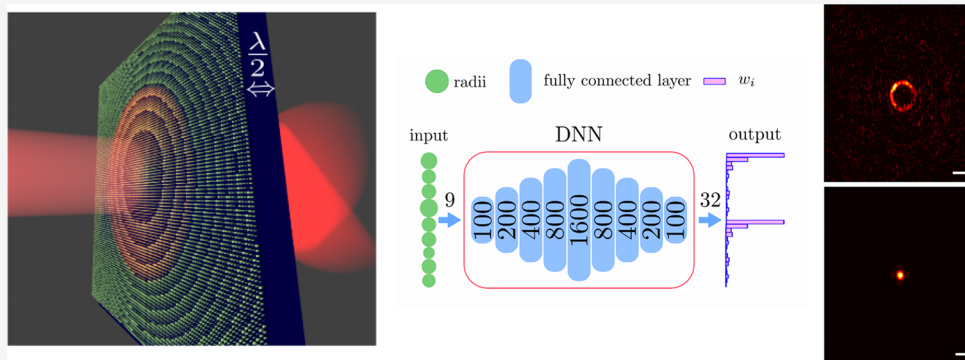
Metrics & More



Article Recommendations



Supporting Information



ABSTRACT: The inverse design of optical metasurfaces is a rapidly emerging field that has already shown great promise in miniaturizing conventional optics as well as developing completely new optical functionalities. Such a design process relies on many forward simulations of a device's optical response in order to optimize its performance. We present a data-driven forward simulation framework for the inverse design of metasurfaces that is more accurate than methods based on the local phase approximation, a factor of 10^4 times faster and requires 15 times less memory than mesh-based solvers and is not constrained to spheroidal scatterer geometries. We explore the scattered electromagnetic field distribution from wavelength scale cylindrical pillars, obtaining low-dimensional representations of our data via the singular value decomposition. We create a differentiable model fitting the input geometries and configurations of our metasurface scatterers to the low-dimensional representation of the output field. To validate our model, we inverse design two optical elements: a wavelength multiplexed element that focuses light for $\lambda = 633$ nm and produces an annular beam at $\lambda = 400$ nm and an extended depth of focus lens.

KEYWORDS: inverse design, dielectric metasurface, multifunctional metasurfaces, computational electromagnetics, deep neural networks, data-driven design

Controlling the optical response of a scatterer via its geometry is the fundamental goal of nanophotonics. In recent years, devices consisting of periodically arranged subwavelength structures, each of which can be engineered to scatter light, have shown promising results in both miniaturizing existing optics^{1,2} as well as in creating elements with new electromagnetic (EM) properties.^{3–8} While such devices, also known as metasurfaces, do provide an extremely large number of parameters for designing optics, it is often challenging to harness all of these degrees of freedom relying solely on intuition. Adapted from the fluid dynamics community,⁹ inverse design provides an alternative paradigm to solve this problem. Here, the quality of a device's performance is characterized by a mathematical figure of merit (FOM). The design method entails running a forward simulation of Maxwell's equations for a specific configuration of the scatterers to calculate the FOM and back-propagating through the physical equations to optimize the FOM and, subsequently, the device's performance by updating the

geometry. Thus, instead of a trial-and-error approach, the large design space is efficiently searched using sophisticated numerical optimization methods. Inverse design has gained considerable interest from the nanophotonics community,¹⁰ and it has already been used to design photonic elements,^{10–12} plasmonic nanostructures,¹³ and metasurfaces.^{14–19} However, inverse design requires running the forward simulation many times, and thus, the ultimate speed of the design depends directly on the computational efficiency of the forward simulation.

Received: September 21, 2020

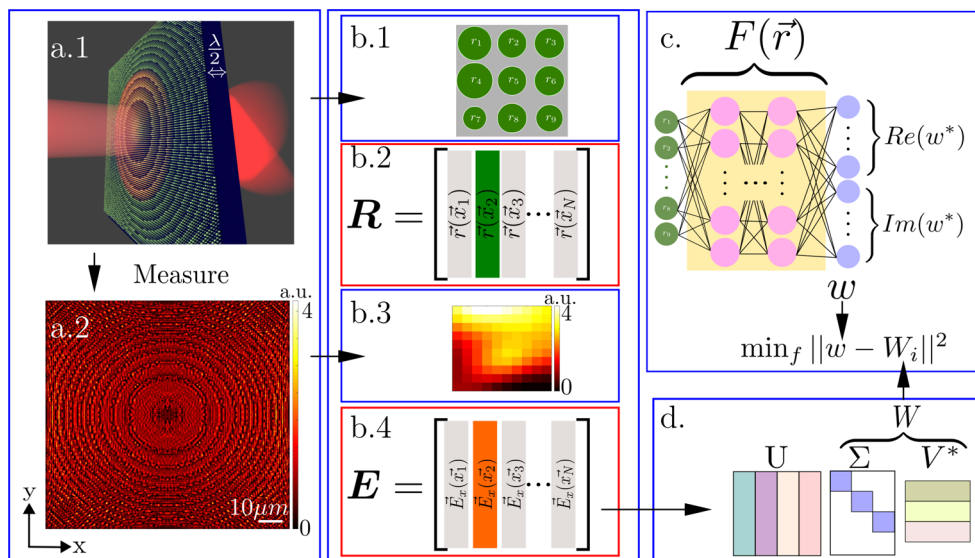


Figure 1. Overview of method. (a.1) Sample forward designed metasurface. (a.2) Near-field response of metasurface for $\lambda = 633$ nm. (b.1–4) Parsing the data. (b.1) Iterate through each pillar except the ones in the edges and gather the surrounding pillar radii. (b.2) Pillar radii and recorded and stacked into matrix R . (b.3) Field response in a square region with dimension of the pitch p corresponding to the central pillar. (b.4) Electric fields are vectorized and stacked into a matrix E . (c) We create a neural network that predicts a vector ω corresponding to the column of matrix. (d) W is constructed as the product ΣV^* , where Σ and V are taken from the SVD of E .

In most existing design methods, Maxwell's equations are solved on a meshed grid, and refractive indices are allowed to change at every point on this grid.^{10–16,20} These methods are accurate and can simulate a scatterer of arbitrary shape; however, they do not scale well to large systems with small features due to the time and memory required to carry out each forward simulation. In contrast, Mie-scattering-based analytical solutions^{17–19} scale better in time and memory, as computational cost only depends on the number of scatterers in each device, but they only work for highly restrictive geometries. To date, only spherical¹⁷ and sparsely packed ellipsoids¹⁸ can be simulated using Mie scattering for inverse design. Another option is to rely on the local phase approximation (LPA),²¹ which assumes the EM properties of a single scatterer can be characterized as a single complex-valued transmission coefficient that is a function of the scatterer geometry and independent from the geometries of the nearby scatterers. This approach requires solving Maxwell's equations under Bloch boundary conditions with methods such as rigorous coupled wave analysis (RCWA).²² Such methods are fast but inaccurate when scatterers on a metasurface are not identical, which is especially apparent when geometries vary rapidly in space or when scatterers are made from materials with low refractive indices.

The objective of this work is to create a forward simulation method for inverse design that is faster than grid-based methods, is not restricted to spheroidal particles, and is more accurate than methods relying on LPA. We will leverage several data-driven modeling and machine learning techniques,²³ which are being adopted in the field of optics and photonics,^{24,25} with examples in fiber lasers^{26–32} and metamaterial antennas.³³

The EM response \vec{E} to an incident current \vec{j} is given by Maxwell's equation:

$$\nabla \times \nabla \times \vec{E}(\mathbf{x}) - \omega^2 \epsilon(\mathbf{x}) \mu(\mathbf{x}) \vec{E}(\mathbf{x}) + i\omega \mu(\mathbf{x}) \vec{j}(\mathbf{x}) = 0 \quad (1)$$

where ω is the angular frequency of the current source, $\epsilon(\mathbf{x})$ is the dielectric permittivity distribution, $\mu(\mathbf{x})$ is the magnetic permeability distribution (assumed to be unity here as we will use dielectric materials), and the vector \mathbf{x} is the position vector.

This implies that the field response $\vec{E}(\mathbf{x})$ only depends on the distribution of $\epsilon(\mathbf{x})$. A forward simulation of Maxwell's equation thus entails the prediction of the spatial EM modes as a function of the scatterer geometry and position. Here, we first use high-fidelity EM simulations to generate data, which are then used to find a simple mapping between $\epsilon(\mathbf{x})$ and $\vec{E}(\mathbf{x})$, exploiting the singular value decomposition (SVD) and neural networks.³⁴ We note that a number of previous works used neural networks to predict the spectral responses from metallic^{35–37} and dielectric^{16,38–43} scatterers of various geometries. In these problems, the unit cells are identical and, hence, there is no need to invoke LPA. However, for imaging applications, where the unit cells are spatially varying, invoking LPA results in inaccuracy. Our work aims to mitigate this challenge by using a data-driven framework to predict the spatial responses from dielectric circular cylinders while including the effects of their nearest neighbors. Another recent work has applied data driven techniques to accelerate iterative finite difference frequency domain (FDFD) solvers.⁴⁴ While accurate, this method is, however, still memory intensive. Our work provides an alternative, interpolative method for simulating field responses from electromagnetic scatterers by fitting a differentiable model that maps the geometry of the scatterer and its closest neighbors to its EM field response. This model speeds up our forward simulation by estimating local patches of the EM field from the radius of a cylindrical scatterer and its surrounding neighbors. We found that this method can simulate a mesh with 1.2 million discrete points 10^4 times faster than conventional grid-based solvers and is memory inexpensive enough that it can be run on a laptop. We use this framework to inverse design two devices, both of which are unintuitive under the forward methodology: a multiwavelength metasurface that produces an annulus beam

for one wavelength and focuses light at a different wavelength as well as an extended depth of focus lens.

METHODS

The goal of this work is to develop a fast and accurate proxy for the forward simulation that is differentiable and may be used for inverse design. Figure 1 shows the schematic of our strategy to build a differentiable map $F: \mathbb{R}^9 \rightarrow \mathbb{C}^{100}$ that predicts the electric field over a square area with dimension p from the dielectric permittivity distribution $\epsilon(\mathbf{x})$, modeled as nine cylinders. Here p is the periodicity of the metasurface, and each square area (unit cell) has been discretized into a 10×10 grid. The corresponding field being predicted is flattened into a 100×1 vector. We will explore two models: a low-dimensional linear regression model based on the singular value decomposition (SVD) and a deep neural network model to fit F .

Training Data. To train these models, we first generate a data set consisting of forward simulations of several physical devices, in our case lenses. These lenses were designed via forward design. The intuition is that the lens is arguably the simplest physical device and will likely provide a useful basis to interpolate future devices. We forward designed 10 lenses of diameter $\sim 50 \mu\text{m}$ with focal lengths varying from 10–100 μm .⁴⁵ The lens design parameters are summarized in Table 1.

Table 1. Parameters Used to Forward Design the Training Data Set^a

parameter	f	D	p	h	n	λ
value	10–100 μm	50.0703 μm	0.4431 μm	0.633 μm	2	0.633 μm

^a f : focal length; h : height of the pillars; n : material index; λ : current source wavelength. The lens diameter D is chosen to be the closest integer multiple of the periodicity p .

All lenses are intended to function with a current source wavelength $\lambda = 0.633 \mu\text{m}$. The material refractive index was set to $n = 2$, corresponding to silicon nitride, our material of choice for visible wavelength operation.⁴⁶ These dimensions correspond to exactly 113 pillars on each axis of the metasurface. All the scatterers were computed with RCWA package S4.²² A sample lens of focal length $f = 50 \mu\text{m}$ is shown in Figure 1a.1. We simulated the EM response of each lens using an x -polarized plane wave ($\lambda = 0.633 \mu\text{m}$) with the field monitor $\lambda/2$ away from the scatterers using Lumerical finite difference time domain (FDTD) software. An example field is shown in Figure 1a.2. Only the \mathcal{E}_x component was recorded

due to minimal contributions to the total field power from other vector components, which is a result of the circular symmetry of the scatterers. However, the process could easily be generalized to predict the entire vector-field. The resolution of the simulation was chosen to be $0.04431 \mu\text{m}/\text{vox}$ in order to balance computational time, memory requirements, and accuracy. This results in (10×10) field points in each square unit cell with a dimension $p = 443 \text{ nm}$ corresponding to each pillar.

Once all of the field data were gathered, we constructed two matrices: $\mathbf{R} \in \mathbb{R}^{9 \times N}$ for the radii and $\mathbf{E} \in \mathbb{C}^{100 \times N}$ for the electric fields, with N being the number of scatterers. The matrix \mathbf{R} was created by iterating over pillar location \mathbf{x}_p and storing the radii of the pillar and its eight nearest neighbors as a column vector, shown in Figure 1b.1 and b.2. The pillars on the edges of the metasurface do not have neighbors and were neglected. Similarly, the matrix \mathbf{E} was created by iterating over each pillar location, extracting the field in the unit cell with centroid \mathbf{x}_p , and storing it as a flattened 100×1 column vector, shown in Figure 1b.3 and b.4. We note that, in this paper, we consider a scalar field, whose polarization axis is the same as the incident polarization. This results in two matrices having $N = (113-2)^2 \times 10 = 123210$ columns.

Linear Regression Model. We first explore the low-dimensional structure of the matrix \mathbf{E} , which will facilitate learning a map between the columns of \mathbf{R} and \mathbf{E} . Patterns in the rows and columns of $\mathbf{E} \in \mathbb{C}^{M \times N}$ are extracted via the singular value decomposition (SVD):³⁴

$$\mathbf{E} = \mathbf{U}\mathbf{\Sigma}\mathbf{V}^* \quad (2)$$

where $\mathbf{U} \in \mathbb{C}^{M \times M}$ and $\mathbf{V} \in \mathbb{C}^{N \times N}$ are unitary matrices, and $\mathbf{\Sigma} \in \mathbb{R}^{M \times N}$ is a diagonal matrix, with non-negative entries on the diagonal and zeros off the diagonal. The columns of \mathbf{U} can be thought of as a set of orthonormal basis vectors with which to represent the columns of \mathbf{E} . These columns of \mathbf{U} are arranged hierarchically in terms of how much variance they capture in \mathbf{E} , as quantified by the corresponding diagonal element of $\mathbf{\Sigma}$. Figure 2a shows the square of the absolute value of the first nine column vectors \mathbf{u}_i , reshaped from $\mathbb{C}^{100 \times 1}$ to $\mathbb{C}^{10 \times 10}$. Definite patterns are observed in these vectors, implying a low-dimensional representation of our data. The rows of \mathbf{V}^* correspondingly provide a hierarchical basis for the rows of \mathbf{E} . Each column of the matrix $\mathbf{\Sigma}\mathbf{V}^*$ determines the exact combination of the columns of \mathbf{U} required to reproduce the corresponding column of \mathbf{E} .

Guided by the SVD, it is possible to write an approximate matrix $\tilde{\mathbf{E}}$ as

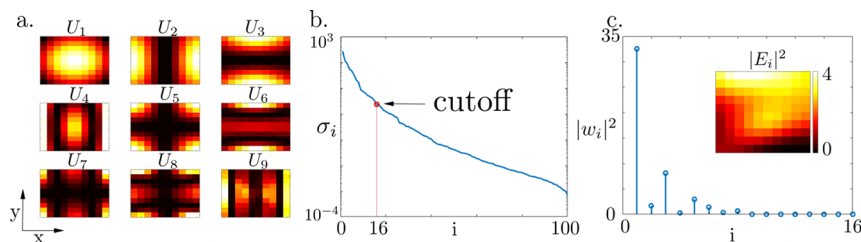


Figure 2. Singular value decomposition of simulated data. (a) First nine left-handed singular vectors \mathbf{U} of \mathbf{E} matrix. (b) Singular value decay of the diagonal matrix $\mathbf{\Sigma}$. Red circle represents the cutoff order we used to reconstruct the electric fields. The order 16 cutoff was chosen because it captures 99% total energy of the electric field. Any further contribution from modes with order $q > 16$ contributes to less than 1% to the total energy in the field. (c) Plot of the absolute values squared of a random vector $(\mathbf{\Sigma}\mathbf{V}^*)_i = \mathbf{w}_i$ that reconstructs some random $p \times p$ field. \mathbf{w}_i represents the weights of the left-hand singular vectors \mathbf{U} .

$$\tilde{\mathbf{E}} = \mathbf{U}_q \mathbf{W} \quad (3)$$

where $\mathbf{W} = \sum_q V_q^*$, and the subscript $q < M$ is the truncation order of the matrix approximation. The first q columns of \mathbf{U} are arranged to form \mathbf{U}_q , the first $q \times q$ sub-block of Σ is extracted to form Σ_q , and the first q rows of V^* are taken to form V_q^* . It can be shown that $\tilde{\mathbf{E}}$ is the best rank q approximation to the matrix \mathbf{E} , in the Frobenius norm.⁴⁷ We choose a truncation value of $q = 16$, shown as the red circle in Figure 2b, as the rank 16 approximation $\tilde{\mathbf{E}}$ captures 99% of the variance in the matrix \mathbf{E} .

We will now construct a regression map to estimate columns of $\tilde{\mathbf{E}}$ from columns of \mathbf{R} . Specifically, we estimate the matrix \mathbf{W} , which will be used to reconstruct $\tilde{\mathbf{E}}$. Instead of using the columns of \mathbf{R} directly as features, we will create an augmented feature vector comprised of monomials constructed from the radii. This feature matrix Θ is constructed by vertically concatenating integer Hadamard powers of \mathbf{R} :

$$\Theta = \begin{bmatrix} 1 \\ \mathbf{R} \\ \mathbf{R}^{\circ 2} \\ \vdots \\ \mathbf{R}^{\circ m} \end{bmatrix} \quad (4)$$

where $\mathbf{R}^{\circ m}$ is the element-wise powers of \mathbf{R} :

$$\mathbf{R}^{\circ m} = \begin{bmatrix} r_{1,1}^m & \cdots & r_{1,N}^m \\ \vdots & \ddots & \vdots \\ r_{M,1}^m & \cdots & r_{M,N}^m \end{bmatrix} \quad (5)$$

Thus, we set up a linear system:

$$\mathbf{W} = \Xi \Theta \quad (6)$$

and solve for Ξ :

$$\Xi \approx \mathbf{W} \Theta^\dagger \quad (7)$$

where the superscript \dagger denotes the Moore–Penrose pseudoinverse.⁴⁷ The matrix $\tilde{\mathbf{E}}$ can then be approximated by a generalized linear regression problem:

$$\tilde{\mathbf{E}} \approx \mathbf{E}_{\text{pred}} = \Xi \Theta \quad (8)$$

We varied the number of features used to train this linear model by changing the number of powers m used to construct Θ . To train this linear model, we used 80% of the data. After creating \mathbf{W} and Θ , we extracted a random set of 98568 columns from each matrix in order to fit the matrix Ξ . We used the other 24642 columns for validation. Figure 3a depicts the qualitative performance of our linear model for $m = 10$. Column I represents a randomly chosen vector \mathbf{E}_i at some position \mathbf{x}_i , column II is the corresponding predicted vector $\mathbf{e}_{\text{pred}} \in \mathbf{E}_{\text{pred}}$, and column III is the absolute difference squared $|e|^2 = |\mathbf{E}_i - \mathbf{e}_{\text{pred}}|^2$. Note that we are comparing complex numbers, while plotting their intensities. Thus, although the intensities may not look extremely similar, their errors can be relatively small. All values were normalized to have a maximum absolute value of 1 and the same color bar across all figures. Figure 3b shows the probability density functions (PDFs) of the error distributions $|\mathbf{E}_{\text{pred}} - \mathbf{E}|^2$ as we increase m from 1 to 10. As the number of features increases, the PDF becomes tighter. Figure 3c is a plot of the relative error defined as

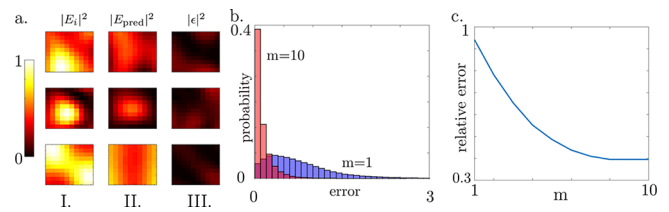


Figure 3. (a) Column I represents the field simulated by FDTD, column II is the electric field predicted using the linear model, and column III is the difference between the two. Each row represents the field corresponding to the same set of 9 radii. (b) Probability density functions of relative errors between the predicted matrix \mathbf{E}_{pred} and the true matrix \mathbf{E} . The blue plot corresponds to a feature matrix with only powers up to 1, and the red plot represents the feature matrix constructed with powers up to 10. (c) Plot of the relative errors in the Frobenius norm between \mathbf{E}_{pred} and \mathbf{E} . The x axis represents the power term in the radius features.

$$\frac{\|\mathbf{E}_{\text{pred}} - \mathbf{E}_{\text{test}}\|_F^2}{\|\mathbf{E}_{\text{test}}\|_F^2} \quad (9)$$

as a function of m . Both plots show the error between our model and the FDTD simulation decreasing as the number of features in each matrix increases, so the model converges to the actual physics of the system. The final relative error for the linear model converged to ≈ 0.395 . As a side note, we have attempted using monomial expansions up to order 2 of column vectors of \mathbf{R} as input features for our model, by using powers of column vectors of \mathbf{R} and cross terms in between radii, but found no significant improvements in relative error when fitting the model.

Neural Network Model. To improve on the generalized linear model, we construct a deep neural network (DNN), shown in Figure 4. We hypothesize that the DNN would learn a nonlinear transformation of the input features that better capture the physics of the system. The model was trained by using 80% of the data set, while keeping 20% for validation. The architecture was implemented in TensorFlow⁴⁸ and optimized using the Adam optimizer.⁴⁹ The DNN architecture consists of 11 fully connected layers, each followed by a ReLU activation function. The first layer of the network is the input layer with 9 neurons corresponding to each radius. The second layer has 100 neurons, which was doubled with each subsequent layer until 1600 and then cut in half until the second to last layer again had 100 neurons. The final layer had 32 neurons, with the first 16 elements corresponding to the real components of the vector \mathbf{w} and the last 16 components corresponding to the imaginary components of \mathbf{w}_i . The outputs were arranged in this manner due to TensorFlow's limitations when designing complex-valued neural networks. The objective function used was a mean squared error between the output vector, and the corresponding vector from \mathbf{W} , shown in detail in Figure 1c,d. The network was trained until the mean squared error of the verification data set stopped being minimized in order to avoid overfitting. Once the network was trained, we computed the electric field response of the training data by feeding the test data set into the neural network to compute \mathbf{W}_{pred} and eq 3 to compute \mathbf{E}_{pred} . The quality of our prediction can again be summarized by the relative error between \mathbf{E}_{pred} and \mathbf{E}_{test} in the Frobenius norm, given in eq 9, which was computed to be ≈ 0.26 . The same metric calculated by using a predicted field from the local

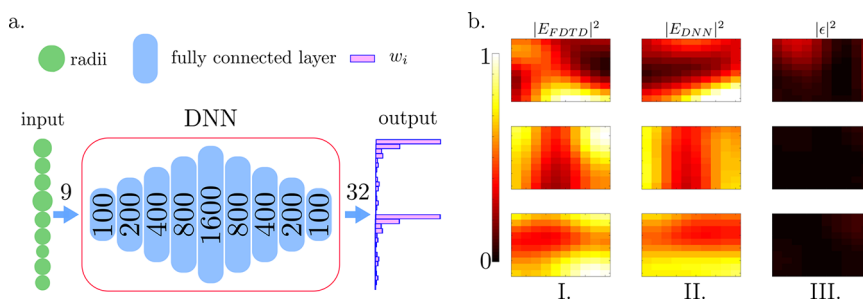


Figure 4. (a) Input into the DNN is 9 radii. The DNN architecture consists of nine fully connected layers. The first layer starts off with 100 neurons, and each subsequent layer doubles the number of neurons until 1600, then number of neurons per layer is halved until the final layer has 100 neurons. All layers are followed by a ReLU activation function. The output has 32 elements. (b) The performance of the DNN model. Column I is the field simulated by FDTD, column II is the field reconstructed by eq 3 from the predicted vector w_p , and column III is the difference between fields.

phase approximation gives a relative error of ≈ 1.35 . We use the DNN model to inverse design our devices. As a side note, the supplement includes a convergence study between number of nearest neighbors included in the neural network model, and the accuracy of the predicted near-field. The relative error of our test data sets turned out to be lowest when using only nearest neighbors.

RESULTS

To test the utility of our model, we inverse designed two meta-optical devices. Motivated by stimulated emission depletion (STED) microscopy,⁵⁰ the first device we inverse designed was a wavelength multiplexed lens that focuses light with $\lambda = 633$ nm, and creates an annulus beam at the focal plane for $\lambda = 400$ nm. The second is an extended depth of focus (EDOF) lens that focuses light over 100–350 μm along the optical axis. The optimization process was implemented in TensorFlow.⁴⁸ We used the DNN model and eq 3 to predict the near-fields of the designed devices. The far-fields were then calculated by using the angular propagation method.⁵¹ The gradients with respect to radii were calculated by using TensorFlow's autodifferentiation, and updated by the adam optimizer.

To design the multiwavelength lens, we had to predict near-fields for two wavelength. Hence, we repeated the procedure outlined in Methods to create one more data driven model to predict the field response for a $\lambda = 400$ nm current source. This model was trained on the same data set as metasurface lenses designed to focus light for the 633 nm wavelength; however, the electric field responses were gathered from FDTD simulations at 400 nm. Once trained, the relative error defined by eq 9 computed on the test data set for $\lambda = 400$ nm was ≈ 0.37 . The difference between the two wavelengths can be explained by the relatively nonsmooth transmission of $\lambda = 400$ nm E-fields over this range of radii when compared to the $\lambda = 633$ nm case. To optimize the lens, we defined two figures of merit for each wavelength as

$$\text{FOM}_{400} = - \sum_{m=0}^{19} I \left(c \cos \left(m \frac{2\pi}{20} \right), c \sin \left(m \frac{2\pi}{20} \right), 50 \mu\text{m} \right) \quad (10)$$

$$\text{FOM}_{633} = -20 \times I(0, 0, 50 \mu\text{m}) \quad (11)$$

where the function $I(x, y, z)$ is the intensity of the electric field at (x, y, z) coordinate given by $I(x, y, z) = \mathcal{E}^*(x, y, z)\mathcal{E}(x, y, z)$. The constant $c = 1.5 \mu\text{m}$, corresponding to the radius of the annular beam at the focal

spot. The tuple $\left(c \cos \left(i \frac{2\pi}{20} \right), c \sin \left(i \frac{2\pi}{20} \right) \right)$ is the parametrization of a circle in the x - y plane that we discretized over 20 points on the circle. The factor of 20 on FOM_{633} is chosen as a normalization factor to ensure the integral of the intensity over the annulus is the same as the intensity at the focal spot. The quantity optimized was then

$$\max(\text{FOM}_{400}, \text{FOM}_{633}) \quad (12)$$

with respect to the radii distribution. We set our initial radius distribution to be the same as the forward designed lens for $\lambda = 633$ nm and $f = 50 \mu\text{m}$. The designed device is shown in Figure 5a. To verify the design, we computed the near-field response

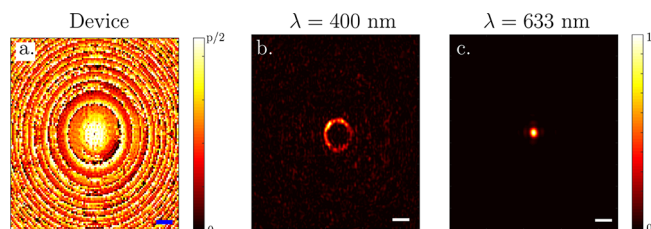


Figure 5. (a) Optimized multifunctional device. Scale bar is 5 μm . (b) FDTD result for $\lambda = 0.4 \mu\text{m}$. (c) FDTD result for $\lambda = 0.633 \mu\text{m}$. Scale bars are 2 μm . Units are normalized so the maximum intensity is equal to 1.

of the radii distribution in Lumerical FDTD and propagated the near-field to the focal plane using angular spectrum method. Figure 5b,c shows the meta-optic's response to 400 and 633 nm wavelengths at the focal plane, respectively. The efficiency η of the metasurface was calculated to be 26.82% for $\lambda = 400$ nm. The formal definition is given in the supplement. We quantify the annulus functionality of the metasurface as the ratio between the power confined in the annulus to the power confined in the center of the annulus. This ratio η_a was calculated to be 58.47 for $\lambda = 633$ nm, formally defined in the supplement.

The ED OF lens was designed by using a lens with $f = 100 \mu\text{m}$ as a starting condition. Our intent was to design an ED OF lens to focus from 50 to 100 μm . We defined the figure of merit for the ED OF as

$$\text{FOM}_{\text{EDOF}} = - \sum_{m=0}^{10} \log(I(0, 0, 50 + m \times dz)) \quad (13)$$

where $dz = 10 \mu\text{m}$. Thus, we aim to maximize the intensity at the center of 10 equispaced x - y planes. The resulting device is shown in Figure 6a. The intent behind the logarithmic sum

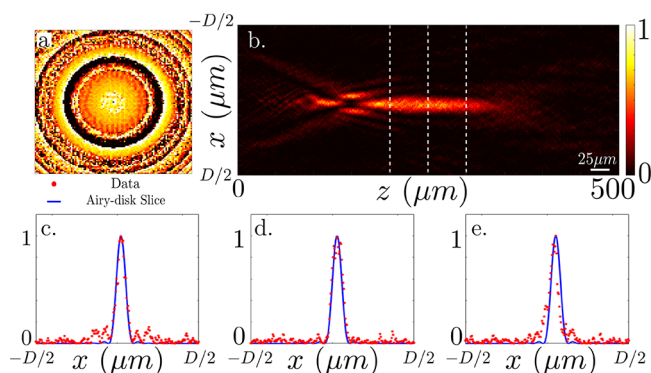


Figure 6. EDOF lens. (a) Device. (b) Simulated field. Simulation is a result of FDTD and angular spectrum propagation. (c–e) Slices of field in (b) along the dashed lines corresponding to 200, 250, and 300 μm , respectively. The red dots are the simulated data. The blue lines are the Airy disk profiles corresponding to the diffraction limit. All intensities are normalized by the corresponding maximum intensity.

was to equalize the importance of each term along the z -axis. Without the logarithm term, the optimization would prioritize a single focal spot, since such a device would minimize the figure of merit. After optimization, this figure of merit converged to a lens focusing from 100 to 350 μm , as shown in Figure 6b, corresponding to a numerical aperture varying from 0.07 to 0.25. We attribute the longer depth of focus than what was intended to the physical nature of wave propagation. Figure 6c–e shows slices of the electric field at 200, 250, and 300 μm along the optical axis. The red dots correspond to the simulated data, and the blue line corresponds to the Airy disk corresponding to the diffraction limited focal spot. We note that clearly there are additional side-lobes in the EDOF design, and thus, the total energy in the main lobe suffers. However, a different figure of merit can be designed to reduce the side-lobes, depending on the desired application.

DISCUSSION

This paper outlines a data driven methodology for the forward simulation of Maxwell's equations to design optical metasurfaces. Our model does not make the local phase approximation, and thus, the interscatterer coupling is well accounted for. While the model is not as accurate as a complete full-wave simulation, it is significantly faster. A single forward simulation of a square area of dimensions $50 \mu\text{m} \times 50 \mu\text{m}$ at 44.31 nm resolution takes approximately 12 s with our method versus approximately 3.1 h using Lumerical FDTD software in the same computer. FDTD also requires a 58.95 GB initialization mesh and 29.6 GB of RAM for the same simulation, while our method only requires 3.75 GB for the same problem and can be run on a mid-range laptop. It takes approximately 16 h to gather the data required for training our neural network model (10 FDTD simulations). Depending on the design problem and based on our results from optimization using our DNN models as a forward simulator, it takes approximately 100 iterations for an inverse design problem to converge. Under these assumptions, we can estimate that we need about 100 forward simulations to do a naive gradient-based design, which would take 310 h to complete by using a

full FDTD simulation. Furthermore, adjoint optimization requires two simulation passes per optimization step, which will make the whole optimization process take at least 620 h. Even when considering the time it takes to gather the data and train our model, the overall design process is sped up significantly. The angular propagation step that transforms the near-fields to the far-fields adds an additional 6 GB of memory and 26 s of optimization time to the optimization per far-field plane used. For the EDOF lens, this results in an additional 60 GB of memory required during the optimization process. We note using a different propagation method such as the Rayleigh–Sommerfeld method that does not require storing the full far-field, but only the field at the point where the FOM is calculated, would significantly reduce the memory requirements for the propagation.

It is worth noting that our method is inherently interpolative and, thus, is only as accurate as the data that we feed into it. Therefore, the current model is limited to predicting fields from lens-like devices, under a specific refractive index, constrained to a subspace of possible geometries. If one wanted to design a metasurface using this method for a different refractive index or with different scatterer geometries, the model would need to be retrained. One way we could improve this model is by using additional data to train it. In our future work, we hope to improve the accuracy of this model by simulating random arrangements of scatterers and using this as our training data set in addition to the data set from lenses. We also emphasize that the reported efficiency of the designed lenses is low, which remains a challenge for low index materials.⁵² However, full-wave simulations have reported an efficiency increase of the metasurface lenses, especially when all the coupling between scatterers are exactly accounted for.^{20,53} Our model could be improved by better accounting for the coupling between scatterers using more data, especially EM field responses from scatterers with rapidly varying geometries, since the scatterer geometries of lenses vary slowly in space. One specific direction will be to capture the physics to predict the full vectorial field, in contrast to the scalar field modeled here. Modeling the second nearest neighboring scatterers could also be an interesting path forward. Utilizing techniques such as transfer learning,⁵⁴ we could utilize the features learned from our previous models that include only information from the nearest scatterers and try to generalize the model for second and even third nearest neighbors. Furthermore, adding additional constraints, such as assumptions about energy conservation to the model training process, could further increase the accuracy of the model.

ASSOCIATED CONTENT

Supporting Information

The Supporting Information is available free of charge at <https://pubs.acs.org/doi/10.1021/acsp Photonics.0c01468>.

Definitions of the efficiency metrics for the designed devices, details about the deep neural network model and its convergence, optimization procedure for inverse design, and model performance for different wavelengths are included (PDF)

AUTHOR INFORMATION

Corresponding Author

Arka Majumdar – Department of Electrical and Computer Engineering and Department of Physics, University of

Washington, Seattle, Washington 98195, United States;
orcid.org/0000-0003-0917-590X; Email: arka@uw.edu

Authors

Maksym V. Zhelyeznyakov – Department of Electrical and Computer Engineering, University of Washington, Seattle, Washington 98195, United States; orcid.org/0000-0002-5814-5857

Steve Brunton – Department of Mechanical Engineering, University of Washington, Seattle, Washington 98195, United States

Complete contact information is available at:
<https://pubs.acs.org/10.1021/acsp Photonics.0c01468>

Notes

The authors declare no competing financial interest.

ACKNOWLEDGMENTS

This research was supported by NSF-1825308, the UW Reality Lab, Facebook, Google, Futurewei, and Amazon. M.Z. is supported by a NSF graduate research fellowship. A.M. is partially supported by Washington Research Foundation distinguished investigator award. S.L.B. acknowledges support from the National Science Foundation (NSF HDR Award #1934292).

REFERENCES

- (1) Zhan, A.; Colburn, S.; Trivedi, R.; Fryett, T. K.; Dodson, C. M.; Majumdar, A. Low-Contrast Dielectric Metasurface Optics. *ACS Photonics* **2016**, *3*, 209–214.
- (2) Wang, S.; et al. A broadband achromatic metalens in the visible. *Nat. Nanotechnol.* **2018**, *13*, 227–232.
- (3) Zhan, A.; Colburn, S.; Dodson, C. M.; Majumdar, A. Metasurface Freeform Nanophotonics. *Sci. Rep.* **2017**, *7*, 1673.
- (4) Colburn, S.; Zhan, A.; Majumdar, A. Varifocal zoom imaging with large area focal length adjustable metalenses. *Optica* **2018**, *5*, 825–831.
- (5) Arbabi, A.; Arbabi, E.; Horie, Y.; Kamali, S. M.; Faraon, A. Planar metasurface retroreflector. *Nat. Photonics* **2017**, *11*, 415–420.
- (6) Arbabi, A.; Horie, Y.; Bagheri, M.; Faraon, A. Dielectric metasurfaces for complete control of phase and polarization with subwavelength spatial resolution and high transmission. *Nat. Nanotechnol.* **2015**, *10*, 937–943.
- (7) Shi, Z.; Khorasaninejad, M.; Huang, Y. W.; Roques-Carnes, C.; Zhu, A. Y.; Chen, W. T.; Sanjeev, V.; Ding, Z.; Tamagnone, M.; Chaudhary, K.; Devlin, R. C.; Qiu, C. W.; Capasso, F. Metasurfaces with wavelength-controlled functions. *Lasers and Electro-Optics* **2018**, JW2A.101.
- (8) Colburn, S.; Zhan, A.; Majumdar, A. Metasurface optics for full-color computational imaging. *Science Advances* **2018**, *4*, eaar2114.
- (9) Jameson, A.; Martinelli, L.; Pierce, N. A. Optimum Aerodynamic Design Using the Navier–Stokes Equations. *Theor. Comput. Fluid Dyn.* **1998**, *10*, 213–237.
- (10) Molesky, S.; Lin, Z.; Piggott, A.; Jin, W.; Vucković, J.; Rodriguez, A. Inverse design in nanophotonics. *Nat. Photonics* **2018**, *12*, 659–670.
- (11) Piggott, A. Y.; Petykiewicz, J.; Su, L.; Vučković, J. Fabrication-constrained nanophotonic inverse design. *Sci. Rep.* **2017**, *7*, 1786.
- (12) Piggott, A. Y.; Lu, J.; Lagoudakis, K. G.; Petykiewicz, J.; Babinec, T. M.; Vučković, J. Inverse design and demonstration of a compact and broadband on-chip wavelength demultiplexer. *Nat. Photonics* **2015**, *9*, 374–377.
- (13) Hansen, P.; Hesselink, L. Accurate adjoint design sensitivities for nano metal optics. *Opt. Express* **2015**, *23*, 23899–23923.
- (14) Pestourie, R.; Pérez-Arancibia, C.; Lin, Z.; Shin, W.; Capasso, F.; Johnson, S. G. Inverse design of large-area metasurfaces. *Opt. Express* **2018**, *26*, 33732–33747.
- (15) Bayati, E.; Pestourie, R.; Colburn, S.; Lin, Z.; Johnson, S. G.; Majumdar, A. Inverse Designed Metalenses with Extended Depth of Focus. *ACS Photonics* **2020**, *7*, 873–878.
- (16) Lin, Z.; Liu, V.; Pestourie, R.; Johnson, S. G. Topology optimization of freeform large-area metasurfaces. *Opt. Express* **2019**, *27*, 15765–15775.
- (17) Zhan, A.; Fryett, T. K.; Colburn, S.; Majumdar, A. Inverse design of optical elements based on arrays of dielectric spheres. *Appl. Opt.* **2018**, *57*, 1437–1446.
- (18) Zhelyeznyakov, M. V.; Zhan, A.; Majumdar, A. Design and optimization of ellipsoid scatterer-based metasurfaces via the inverse T-matrix method. *OSA Continuum* **2020**, *3*, 89–103.
- (19) Zhan, A.; Gibson, R.; Whitehead, J.; Smith, E.; Hendrickson, J. R.; Majumdar, A. Controlling three-dimensional optical fields via inverse Mie scattering. *Science Advances* **2019**, *5*, eaax4769.
- (20) Mansouree, M.; Kwon, H.; Arbabi, E.; McClung, A.; Faraon, A.; Arbabi, A. Multifunctional 2.5D metastructures enabled by adjoint optimization. *Optica* **2020**, *7*, 77–84.
- (21) Hsu, L.; Dupré, M.; Ndao, A.; Yellowhair, J.; Kanté, B. Local phase method for designing and optimizing metasurface devices. *Opt. Express* **2017**, *25*, 24974–24982.
- (22) Liu, V.; Fan, S. S⁴: A free electromagnetic solver for layered periodic structures. *Comput. Phys. Commun.* **2012**, *183*, 2233–2244.
- (23) Brunton, S. L.; Kutz, J. N. *Data-Driven Science and Engineering: Machine Learning, Dynamical Systems, and Control*; Cambridge University Press, 2019.
- (24) Zibar, D.; Wymeersch, H.; Lyubomirsky, I. Machine learning under the spotlight. *Nat. Photonics* **2017**, *11*, 749–751.
- (25) Won, R. Intelligent learning with light. *Nat. Photonics* **2018**, *12*, 571–573.
- (26) Fu, X.; Brunton, S. L.; Nathan Kutz, J. Classification of birefringence in mode-locked fiber lasers using machine learning and sparse representation. *Opt. Express* **2014**, *22*, 8585–8597.
- (27) Brunton, S. L.; Fu, X.; Kutz, J. N. Self-Tuning Fiber Lasers. *IEEE J. Sel. Top. Quantum Electron.* **2014**, *20*, 464.
- (28) Andral, U.; Fodil, R. S.; Amrani, F.; Billard, F.; Hertz, E.; Grellu, P. Fiber laser mode locked through an evolutionary algorithm. *Optica* **2015**, *2*, 275–278.
- (29) Andral, U.; Buguet, J.; Fodil, R. S.; Amrani, F.; Billard, F.; Hertz, E.; Grellu, P. Toward an autotuning mode-locked fiber laser cavity. *J. Opt. Soc. Am. B* **2016**, *33*, 825–833.
- (30) Woodward, R.; Kelleher, E. J. Towards “smart lasers”: self-optimization of an ultrafast pulse source using a genetic algorithm. *Sci. Rep.* **2016**, *6*, 37616.
- (31) Baumeister, T.; Brunton, S. L.; Kutz, J. N. Deep learning and model predictive control for self-tuning mode-locked lasers. *J. Opt. Soc. Am. B* **2018**, *35*, 617–626.
- (32) Sun, C.; Kaiser, E.; Brunton, S. L.; Kutz, J. N. Deep reinforcement learning for optical systems: A case study of mode-locked lasers. *Mach. Learn.: Sci. Technol.* **2020**, *1*, 045013.
- (33) Johnson, M. C.; Brunton, S. L.; Kundtz, N. B.; Kutz, J. N. Extremum-seeking control of a beam pattern of a reconfigurable holographic metamaterial antenna. *J. Opt. Soc. Am. A* **2016**, *33*, 59–68.
- (34) Brunton, S. L.; Kutz, J. N. *Data-Driven Science and Engineering: Machine Learning, Dynamical Systems, and Control*; Cambridge University Press, 2019; pp i–iv.
- (35) Malkiel, I.; Mrejen, M.; Nagler, A.; Arieli, U.; Wolf, L.; Suchowski, H. Plasmonic nanostructure design and characterization via Deep Learning. *Light: Sci. Appl.* **2018**, *7*, 60.
- (36) Li, X.; Shu, J.; Gu, W.; Gao, L. Deep neural network for plasmonic sensor modeling. *Opt. Mater. Express* **2019**, *9*, 3857–3862.
- (37) Ma, W.; Cheng, F.; Liu, Y. Deep-Learning-Enabled On-Demand Design of Chiral Metamaterials. *ACS Nano* **2018**, *12*, 6326–6334.

- (38) Peurifoy, J.; Shen, Y.; Jing, L.; Yang, Y.; Cano-Renteria, F.; DeLacy, B. G.; Joannopoulos, J. D.; Tegmark, M.; Soljačić, M. Nanophotonic particle simulation and inverse design using artificial neural networks. *Science Advances* **2018**, *4*, eaar4206.
- (39) Kiarashinejad, Y.; Zandehshahvar, M.; Abdollahramezani, S.; Hemmatyar, O.; Pourabolghasem, R.; Adibi, A. Knowledge Discovery in Nanophotonics Using Geometric Deep Learning. *Advanced Intelligent Systems* **2020**, *2*, 1900132.
- (40) So, S.; Badloe, T.; Noh, J.; Bravo-Abad, J.; Rho, J. Deep learning enabled inverse design in nanophotonics. *Nanophotonics* **2020**, *9*, 1041–1057.
- (41) Liu, D.; Tan, Y.; Khoram, E.; Yu, Z. Training Deep Neural Networks for the Inverse Design of Nanophotonic Structures. *ACS Photonics* **2018**, *5*, 1365–1369.
- (42) Gao, L.; Li, X.; Liu, D.; Wang, L.; Yu, Z. A Bidirectional Deep Neural Network for Accurate Silicon Color Design. *Adv. Mater.* **2019**, *31*, 1905467.
- (43) An, S.; Fowler, C.; Zheng, B.; Shalaginov, M. Y.; Tang, H.; Li, H.; Zhou, L.; Ding, J.; Agarwal, A. M.; Rivero-Baleine, C.; Richardson, K. A.; Gu, T.; Hu, J.; Zhang, H. A Novel Modeling Approach for All-Dielectric Metasurfaces Using Deep Neural Networks. *arXiv:1906.03387 [physics.optics]* **2019**, na.
- (44) Trivedi, R.; Su, L.; Lu, J.; Schubert, M. F.; Vuckovic, J. Data-driven acceleration of photonic simulations. *Sci. Rep.* **2019**, *9*, 19728.
- (45) Chen, H.-T.; Taylor, A.; Yu, N. A review of metasurfaces: Physics and applications. *Rep. Prog. Phys.* **2016**, *79*, 076401.
- (46) Colburn, S.; Zhan, A.; Bayati, E.; Whitehead, J.; Ryou, A.; Huang, L.; Majumdar, A. Broadband transparent and CMOS-compatible flat optics with silicon nitride metasurfaces [Invited]. *Opt. Mater. Express* **2018**, *8*, 2330–2344.
- (47) Trefethen, L. N.; Bau, D. *Numerical Linear Algebra*; SIAM, 1997.
- (48) Abadi, M., et al. TensorFlow: Large-Scale Machine Learning on Heterogeneous Systems. 2015; Software available from <https://www.tensorflow.org/>.
- (49) Kingma, D. P.; Ba, J. et al. Adam: A method for stochastic optimization. *arXiv preprint arXiv:1412.6980* 2014,.
- (50) Vicidomini, G.; Bianchini, P.; Diaspro, A. STED super-resolved microscopy. *Nat. Methods* **2018**, *15*, 173–182.
- (51) Goodman, J. W. *Introduction to Fourier optics*, 3rd ed.; Roberts & Co. Publishers, 2005; Englewood, CO, 2005; Vol. 1.
- (52) Bayati, E.; Zhan, A.; Colburn, S.; Zhelyeznyakov, M. V.; Majumdar, A. Role of refractive index in metalens performance. *Appl. Opt.* **2019**, *58*, 1460–1466.
- (53) Chung, H.; Miller, O. D. High-NA achromatic metalenses by inverse design. *Opt. Express* **2020**, *28*, 6945–6965.
- (54) Zhuang, F.; Qi, Z.; Duan, K.; Xi, D.; Zhu, Y.; Zhu, H.; Xiong, H.; He, Q. A Comprehensive Survey on Transfer Learning. *Proc. IEEE* **2021**, *109*, 43.